The Astrophysical Journal, 679: L155–L159, 2008 June 1

NON-GAUSSIAN LINE PROFILES IN A LARGE SOLAR FLARE OBSERVED ON 2006 DECEMBER 13

S. Imada,[1] H. Hara,[1] T. Watanabe,[1] A. Asai,[2] T. Minoshima,[3] L. K. Harra,[4] and J. T. Mariska[5]

Received 2008 February 13; accepted 2008 April 16; published 2008 May 2

ABSTRACT

We have studied the characteristics of the non-Gaussian line profile of the Fe xiv 274.20 Å line in and around a flare arcade. We found that broad non-Gaussian line profiles associated with redshifts are observed in the flare arcade. There were two typical types of broad line profiles. One was a distorted line profile caused by multiple flows, and the other was a symmetric line profile without any additional component. We successfully distinguished those two types using higher order statistical moments or *M*—the additional component contribution—defined in this Letter. The distorted/symmetric broad line profiles were preferentially observed in new/old flare loops, respectively.

Subject headings: Sun: corona — Sun: flares

1. INTRODUCTION

Understanding the processes that convert stored free magnetic energy in the corona to thermal energy and kinetic energy or nonthermal particle energy is important for understanding the physics of solar flares. One of the most likely mechanisms for explaining such rapid energy conversion is magnetic reconnection. Modern telescope observations have confirmed many typical features expected from the magnetic reconnection model (e.g., Tsuneta et al. 1992; Yokoyama et al. 2001; Ohyama & Shibata 1998; Teriaca et al. 2003). It is well known that some part of the thermal and nonthermal particle energy reaches to the chromosphere where it causes a sudden increase in the temperature. The overpressure of the chromospheric plasma then drives material into corona in an upward flow—the chromospheric evaporation flow. The density in the flare loop increases with this flow, and the energy in the plasma is lost by radiation in the high-density environment (e.g., Cargill et al. 1995). On the other hand, kinetic energy can also be converted to thermal energy by the fast mode shock which is thought to be located downstream of the reconnection outflow. Although the fast shock is observed in many MHD simulations (e.g., Yokoyama & Shibata 2001), there is little observational evidence for its existence.

It is also plausible that kinetic energy is converted into wave or turbulent energy which is expected to be observed as nonthermal broadening of emission lines (Doschek et al. 1997). There are many previous solar flare studies that aim to understand the observed nonthermal broadening of soft X-ray emission lines which are emitted from ~10 MK plasma (e.g., Doschek et al. 1996; Harra-Murnion et al. 1997). Mariska (1994) discusses the center-to-limb dependence of the nonthermal broadening using data from the Bragg Crystal Spectrometer (BCS) on the *Yohkoh* spacecraft, and found no clear dependence. This observation indicates that the nonthermal broadening is isotropic. Mariska & McTiernan (1999) also discuss the difference between limb flares for which the footpoints were occulted and unocculted, and concluded that occulted limb flares are indistinguishable from unocculted limb flares. This result indicates that the high-temperature emission sources at footpoints do not contribute to the observed nonthermal broadening. Although considerable effort has been devoted toward understanding nonthermal broadening in flaring plasma, its role in the flare process is still unclear.

In this Letter, we focus on the EUV line profiles observed in flaring loops around the impulsive phase of a *GOES* X3.2 flare on 2006 December 13 with the EUV Imaging Spectrometer (EIS) on the recently launched *Hinode* spacecraft. Our motivation in this Letter is to determine the broad non-Gaussian line profile region in the flare loop and to understand their typical characteristics using EIS observation. We believe that our study can contribute to the understanding of the role of nonthermal broadening in solar flare.

2. OBSERVATION AND DATA ANALYSIS

EIS on board *Hinode* is a high spectral resolution spectrometer aimed at studying dynamic phenomena in the corona with high spatial resolution and sensitivity (Culhane et al. 2007). While making a large raster scan from 01:12 to 05:42 UT on 2006 December 13, EIS observed an X3.2 flare.

Data from the raster were processed using the EIS-team-provided software (EIS_PREP), which corrects for flat field, dark current, cosmic rays, and hot pixels, and applies a prelaunch photometric calibration to the data. An orbital variation of the line position was also corrected in the manner described by Imada et al. (2007). Unfortunately, most of the strong emission lines formed at high temperatures such as those of Fe xv and Ca xvii were saturated because of the size of the flare. Thus we used data from the Fe xiv line at 274.20 Å ($\log T = 6.3$) in this Letter.

Figure 1 shows the Fe xiv intensity map with the Doppler velocity (*red and blue contours*) and the line width (*green contours*) obtained from EIS. The horizontal/vertical axes show the solar location in arcseconds. The red/blue contours represent red/blueshifts, respectively (level: 25 km s^{-1}). The green contours show a 60 km s^{-1} level of line width in standard deviation. We can clearly see that the broad line profiles are mostly associated with Doppler velocity. Unfortunately, we cannot understand the time evolution of this flow and line broadening from the raster scanning observation only. Let us compare the EIS observation with other observations. Panels

[1] National Astronomical Observatory of Japan, 2-21-1 Osawa, Mitaka-shi, Tokyo 181-8588, Japan.
[2] Nobeyama Solar Radio Observatory, Minamisaku, Nagano 384-1305, Japan.
[3] Department of Earth and Planetary Science, University of Tokyo, 7-3-1 Hongo, Bunkyo-ku, Tokyo 113-0033, Japan.
[4] UCL–Mullard Space Science Laboratory, Holmbury St. Mary, Dorking, Surrey RH5 6NT, UK.
[5] Space Science Division, Naval Research Laboratory, Washington, DC 20375.

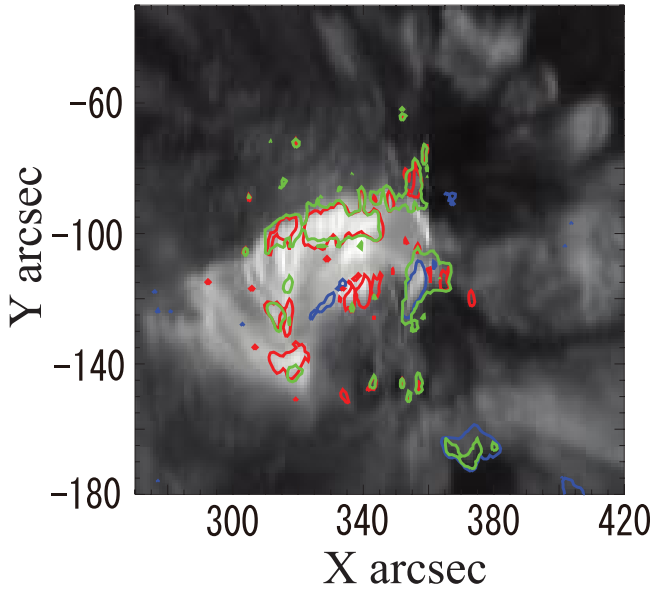

FIG. 1.—EIS Fe XIV flare intensity map (*colors*) with the Doppler velocity (*red and blue contours*; level = 25 km s^{-1}) and the line width (*green contours*; level = 60 km s^{-1}).

a and *b* of Figure 2 (Plate 1) show the *GOES* X-ray (1.0–8.0 Å) light curve and the Nobeyama Radio Polarimeters (NoRP 35 GHz; Nakajima et al. 1985 and references therein) signal. Note that UT starts on the right side and ends on the left side. Figures 2*c*–2*e* show a time series of X-ray images obtained by X-Ray Telescope (XRT) on board *Hinode*. The contours show the Doppler shifts, which are the same as in Figure 1. We coaligned between EIS and XRT by doing a correlation analysis between the EIS Fe XIV intensity map and an XRT thin beryllium filter image in the nonflaring region, which is located in upper right part of Figure 2*c*. The observing times for the EIS raster are shown at the top of Figure 2*a*. Note that EIS raster scanning starts from the west side (right-hand side in Figs. 2*c*–2*e*) and goes to the east side (left-hand side). The orange dashed lines show the slit position of EIS scanning in the XRT image at 02:16:18, 02:27:19, and 02:39:19.

In Figure 2*a* we can see that the flare onset occurred around 02:15 and that the *GOES* X-ray peak was around 02:40. The strong enhancement of the *GOES* X-ray was observed from 02:20 to 02:30 with NoRP enhancements which correspond to the impulsive phase (Fig. 2*b*). Thus, the XRT images of Figures 2*c*–2*e* correspond to the flare onset, the impulsive phase, and the *GOES* maximum, respectively. During the impulsive phase, a strong blueshift was observed around solar $X \sim 360''$ and solar $Y \sim -120''$ which was discussed in Asai et al. (2008). From their analysis these blueshifts are associated with plasmoid ejections during the impulsive phase. Small redshift regions were also observed from the flare onset to the end of impulsive phase. We do not discuss those features during the impulsive phase in detail (see Asai et al. 2008). Our study concentrates on the flare loops just after impulsive phase in this Letter. From the end of the impulsive phase, we observed two redshift regions in the flare arcade. We found that those two correspond to the footpoints/flare ribbons of the flaring loops by comparing the Ca II image obtained by Solar Optical Telescope on board the *Hinode* spacecraft (not shown here), although there is some ambiguity in height from the solar surface (e.g., Czaykowska et al. 1999). In particular, the northern part shows strong redshifts, and in this Letter we refer to this as the northern redshift region (NRR) (Fig. 2*d*). Weak blueshifts were also observed at this stage around solar $X \sim 330''$ and solar $Y \sim -130''$.

Figures 2*f*–2*j* show the Fe XIV line profile in and around the flare loops. The yellow arrows in Figure 2*c* show the locations at which the line profiles were obtained. In Figures 2*f*–2*l* the black solid lines with error bars show the Fe XIV line profiles obtained by EIS. The black dashed line marks the rest wavelength of the Fe XIV 274.204 Å line. The blue/red solid lines show the fitting results with single/double Gaussians, respectively. The fitting functions are as follows:

$$f_s(\lambda) = a_0 \exp\left[-\frac{(\lambda-\mu_0)^2}{2\sigma_0^2}\right] + C_0, \tag{1a}$$

$$f_d(\lambda) = a_1 \exp\left[-\frac{(\lambda-\mu_1)^2}{2\sigma_1^2}\right] + a_2 \exp\left[-\frac{(\lambda-\mu_2)^2}{2\sigma_2^2}\right] + C_1, \tag{1b}$$

where f_s and f_d are the single- and double-Gaussian fitting functions, respectively, and a_i, μ_i, σ_i, and C_i ($i = 0, 1, 2$) are the fitting parameters. For cases where the reduced χ^2 value of the single-Gaussian fit exceeded 4.5, we fit the line profile with a double Gaussian. The orange and pink dashed lines show the two components of the double-Gaussian fitting. The fitting results are summarized in Table 1. We chose a_1 and a_2 to meet the condition $a_1\sigma_1 \geq a_2\sigma_2$.

In Figure 2*f* a strong redshift (~140 km s^{-1}) with a stationary component can be seen. No blueshifted component is visible in this line profile. Note that the spectral line in Figure 2*f* was obtained in the preflare stage. It is plausible that chromospheric evaporation was not yet occurring in this early stage of the flare. The broad redshifted component (~60 km s^{-1}) with blueshift (~40 km s^{-1}) can be seen in the impulsive phase (Fig. 2*g*). At the peak time of the *GOES* flux, we can see both a flat-topped and a sharply peaked line profile in Figures 2*h* and 2*i*, respectively. In Figure 2*j* the line profile is blueshifted without strong line broadening. From those spectral lines, we can clearly see that there are two typical types of the broad line

TABLE 1
FITTING RESULTS BY SINGLE AND DOUBLE GAUSSIAN

Position	a_0	μ_0	σ_0	χ^2	a_1	μ_1	σ_1	a_2	μ_2	σ_2
f	6015	274.223	0.078	4.98	6875	274.202	0.056	2926	274.330	0.032
g	88465	274.214	0.063	103	85524	274.170	0.033	54966	274.256	0.058
h	65784	274.251	0.095	17.1	62727	274.209	0.068	37339	274.340	0.051
i	51057	274.213	0.083	15.6	31073	274.219	0.103	27001	274.208	0.044
j	32565	274.164	0.039	3.02	...	...	...	...	...	...

NOTES.—The terms a_i, μ_i, and σ_i ($i = 0, 1, 2$) show the intensity (ergs cm^{-2} s^{-1} sr^{-1} Å^{-1}), line center position (Å), and standard deviation (Å).

TABLE 2
STATISTICAL MOMENTS

Position	Mean	Standard Deviation	Skewness	Kurtosis	M
f	274.227	0.073	0.1886	−0.549	0.0311
g	274.215	0.064	0.5087	−0.262	0.0963
h	274.249	0.087	0.0218	−0.556	0.0591
i	274.215	0.090	−0.0003	0.462	−0.0041

profiles. One is a distorted line profile caused by multiple flow speeds such as in Figures 2*f*–2*h*, and the other is a symmetric line profile without any flow component (Fig. 2*i*) (e.g., Winebarger et al. 2002). To distinguish these two types, we calculated the higher order moments and the additional component contribution to the line broadening which defined as follows:

$$M \equiv \frac{a_2\sigma_2}{a_1\sigma_1}(\mu_2 - \mu_1). \quad (2)$$

Note that we do not use the data itself to calculate the higher order moments. Instead we use the results of the double-Gaussian fitting. Table 2 shows the results of the moment calculation along with the additional component contribution index. The line profiles at positions *f*–*h* show a large positive skewness, which is a consequence of the significant contribution of the tail on the redshift side. They also show a large negative kurtosis, reflecting the flat-topped line profile. On the other hand, the line profile at position *i* shows a small skewness and large positive kurtosis. This result indicates that the line profile is symmetric and sharply peaked. The additional component contribution index M also clearly distinguishes these two types of line broadening. Although the skewness and kurtosis are good indicators of these two types, in this Letter we use M to discuss where and when these two types were preferentially observed.

In Figure 3 we show a map of the additional component contribution index M larger/smaller than $+/-0.03$ by using orange (positive)/light blue (negative) colors, respectively. The area marked in green shows the broad line profile region (>60 km s^{-1} in standard deviation), and is overlaid by orange or light blue. The black dashed lines show the same times as the orange lines in Figures 2*c*–2*g*. Note that M is calculated only in the region where the value of the reduced χ^2 exceeded 4.5 (inside the white line). Thus the green region inside the white line represents the broad line profile without any large contribution by multiple flow speed. The orange/green region was preferentially observed in the west/east part of the NRR, respectively.

3. DISCUSSION AND SUMMARY

We have examined the characteristics of the broad non-Gaussian line profile of the Fe XIV 274.20 Å line in and around a flare arcade. We found that (1) broad non-Gaussian line profiles associated with redshifts were observed in the flare arcade, (2) there were two typical types (symmetric and distorted) of broad line profiles, (3) those two types were clearly distinguished by higher order statistical moments or M defined in the present Letter, and (4) the symmetric/distorted broad line profiles were located in the east/west part of the NRR, respectively.

There are two important points regarding the location of symmetric and distorted broad line profiles in the flare arcade in Figure 3. First, the distorted broad line profiles (*orange region*) were preferentially observed in the western part of the

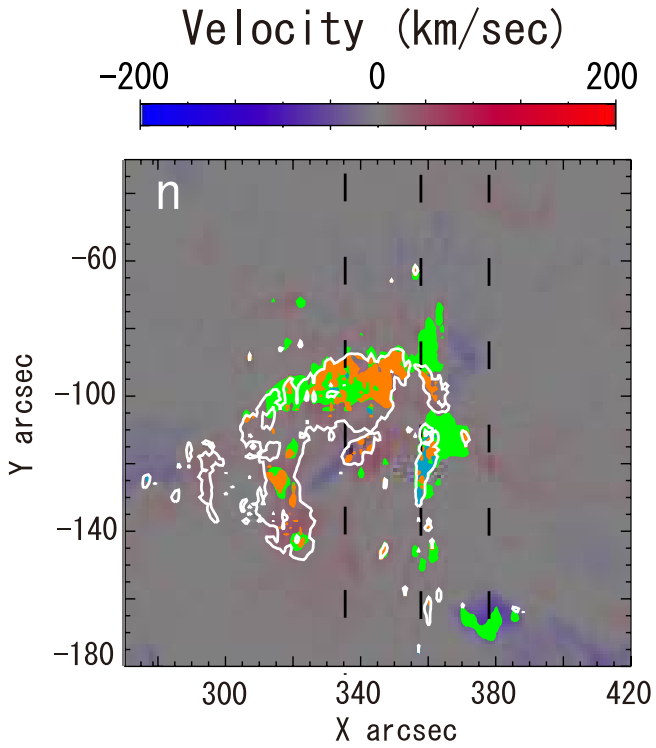

FIG. 3.—Location of distorted (*orange*) and symmetric (*green*) broad line profiles. Location of reduced $\chi^2 > 4.5$ (single-Gaussian fitting) is also shown (*white line*). Note that we calculate the distortion (M) only inside the white lines. The black dashed lines show the same times as the orange dashed lines in Figs. 2*a*–2*e*.

NRR. Although Figure 3 shows the spatial location of the distorted broad line profiles, since EIS is rastering, it also represents the time evolution of line profiles. Thus Figure 3 can also be interpreted as the time series of the line profiles. It is possible that the distorted broad line profiles were preferentially observed from just after the impulsive phase, and the symmetric broad line profiles were observed after the time of the *GOES* peak flux. Second, the distorted broad line profiles were preferentially observed not only on the west side but also on the north side of the NRR. Previous studies of this flare have shown the details of the soft X-ray flare loop structure and the flare ribbons' development (e.g., Yan et al. 2007; Isobe et al. 2007). Their results show that the structure developed in the north-south direction, forming the flare arcade in a large sense. Thus the north/south parts of the NRR correspond to new/old loop footpoints. Both of those two points indicate that the distorted/symmetric broad line profiles were preferentially observed in new/old flare loops, respectively. Our observed large pictures are summarized in Figure 4.

The time evolutions of spectroscopic measurements in the footpoints of on-disk flares have been studied using *SOHO* CDS observations (e.g., Brosius 2003; Brosius & Phillips 2004). Brosius (2003) also shows the down flow ($T \sim 100$ MK), which is called "warm rain," just after the impulsive phase, although these results have some spatial ambiguity (sit-and-stare observation). In Figure 3 we can see that the small filamented structures which show the distorted line profile (*orange*) penetrate into the region of the symmetric line profiles (*green*). We think those lacking in uniformity are caused by the variation of flare condition at each loop. EIS successfully resolved these fine structures because of its high spatial reso-

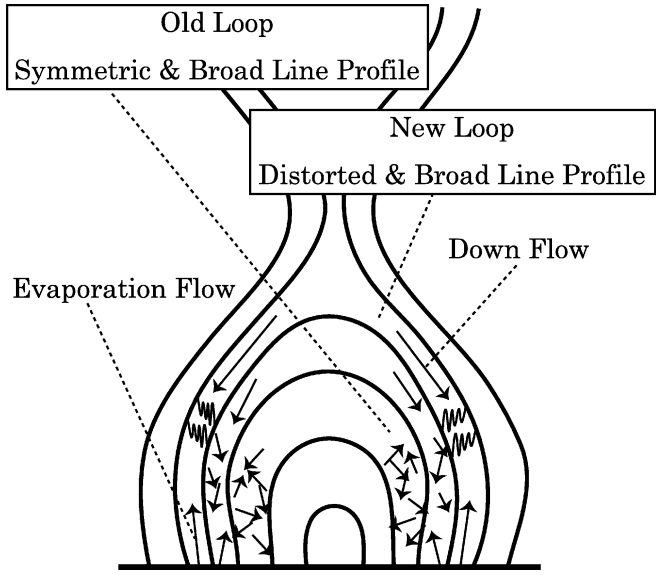

FIG. 4.—Schematic illustration of the observation results. The arrows represent the velocities.

lution. The spectroscopic observation with the high spatial resolution is crucial to discuss the line broadening. Actually, both of the line profiles in Figures 2*h* and 2*i* are observed roughly at the same times (1 minute) and positions (2″). However, their spectral shapes are quite different.

For the limb flare observation, Hara et al. (2006) have discussed the increase with time of the loop-top nonthermal line width in a small flaring event using an Fe XXVI emission line and they concluded that the increase of the nonthermal line width starts when the line intensity reaches its peak. Mariska & McTiernan (1999) have also shown the nonthermal broadening velocity as a function of time using a Ca XIX emission line. They concluded that the peak in the nonthermal broadening velocity occurs after the first significant hard X-ray peak. Their conclusion is consistent with our scenario (Fig. 4), although our observation is different from their study in temperature, *GOES* class, and flare location. The impacts of these differences on the nonthermal broadening are topics of future works.

Finally, we discuss the reason that the older flare loops show symmetric broad line profiles. In most flare models, the conduction front and the nonthermal particles reach the chromosphere earlier than the reconnection outflow. The collision site between the reconnection flow and the evaporation flow may be turbulent because of its large velocity gap. For example, Yokoyama & Shibata (2001) found in a magnetohydrodynamic simulation that a high-density hump is formed at the collision site. Additional simulations and observations should further clarify the origin of the symmetric broad line profiles.

The authors thank T. Yokoyama, K. Shibasaki, S. Nitta, and M. Yamada for fruitful discussions. *Hinode* is a Japanese mission developed and launched by ISAS/JAXA, with NAOJ as domestic partner and NASA and STFC (UK) as international partners. This work was supported in part by the Grant-in-Aid for Creative Scientific Research of MEXT/Japan, the Basic Study of Space Weather Predication.

REFERENCES

Asai, A., et al. 2008, ApJ, submitted
Brosius, J. W. 2003, ApJ, 586, 1417
Brosius, J. W., & Phillips, K. J. H. 2004, ApJ, 613, 580
Cargill, P. J., Mariska, J. T., & Antiochos, S. K. 1995, ApJ, 439, 1034
Culhane, J. L., et al. 2007, Sol. Phys., 243, 19
Czaykowska, A., et al. 1999, ApJ, 521, L75
Doschek, G. A., Mariska, J. T., & Sakao, T. 1996, ApJ, 459, 823
Doschek, G. A., et al. 2007, ApJ, 667, L109
Hara, H., Nishino, Y., Ichimoto, K., & Delaboudiniere, J. P. 2006, ApJ, 648, 712
Harra-Murnion, L. K., Akita, K., & Watanabe, T. 1997, ApJ, 479, 464
Imada, S., et al. 2007, PASJ, 59, S793
Isobe, H., et al. 2007, PASJ, 59, S807
Mariska, J. 1994, ApJ, 434, 756
Mariska, J. T., & McTiernan, J. M. 1999, ApJ, 514, 484
Nakajima, H., et al. 1985, PASJ, 37, 163
Ohyama, M., & Shibata, K. 1998, ApJ, 499, 934
Teriaca, L., et al. 2003, ApJ, 588, 596
Tsuneta, S., et al. 1992, PASJ, 44, L63
Winebarger, A. R., et al. 2002, ApJ, 565, 1298
Yan, Y., Huang, J., Chen, B., & Sakurai, T. 2007, PASJ, 59, S815
Yokoyama, T., Akita, K., Morimoto, T., Inoue, K., & Newmark, J. 2001, ApJ, 546, L69
Yokoyama, T., & Shibata, K. 2001, ApJ, 549, 1160

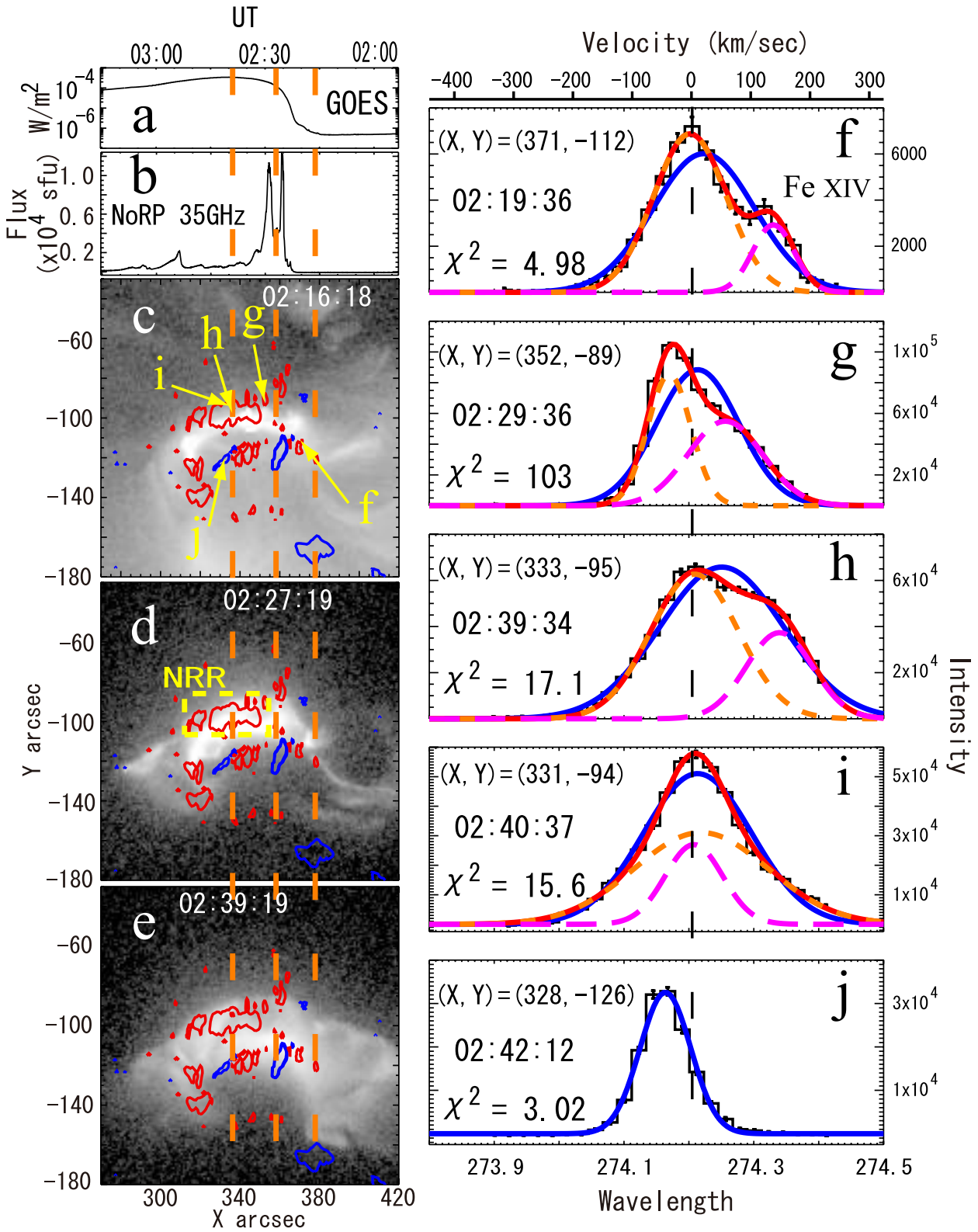

PLATE 1

FIG. 2.—Time profile of (*a*) *GOES* and (*b*) NoRP on 2006 December 13. (*c–e*) Time series of XRT images with Doppler shift contours. (*f–j*) Fe XIV line profiles in and around the flare arcade. The orange dashed lines in (*a–e*) are 02:16, 02:27, and 02:39 from the right, respectively. The black dashed line in (*f–j*) shows the rest wavelength of the Fe XIV line.